Magnetic Fields in Massive Star-forming Regions (MagMaR). V. The Magnetic Field at the Onset of High-mass Star Formation

Patricio Sanhueza[1,2,3,35] , Junhao Liu (刘峻豪)[2] , Kaho Morii[2,4] , Josep Miquel Girart[5,6] , Qizhou Zhang[7] ,
Ian W. Stephens[8] , James M. Jackson[9] , Paulo C. Cortés[10,11] , Patrick M. Koch[12] , Claudia J. Cyganowski[13] ,
Piyali Saha[2] , Henrik Beuther[14] , Suinan Zhang (张遂楠)[15] , Maria T. Beltrán[16] , Yu Cheng[2] , Fernando A. Olguin[2,17,18] ,
Xing Lu (吕行)[15] , Spandan Choudhury[19] , Kate Pattle[20] , Manuel Fernández-López[21] , Jihye Hwang[19] ,
Ji-hyun Kang[19] , Janik Karoly[20] , Adam Ginsburg[22] , A.-Ran Lyo[19] , Kotomi Taniguchi[2] , Wenyu Jiao[15] ,
Chakali Eswaraiah[23] , Qiu-yi Luo (罗秋怡)[15,24,25] , Jia-Wei Wang[12,26] , Benoît Commerçon[27] , Shanghuo Li[28,29] ,
Fengwei Xu[30,31,32] , Huei-Ru Vivien Chen[18] , Luis A. Zapata[33] , Eun Jung Chung[19] , Fumitaka Nakamura[2,4] ,
Sandhyarani Panigrahy[23] , and Takeshi Sakai[34]

[1] Department of Earth and Planetary Sciences, Institute of Science Tokyo, Meguro, Tokyo 152-8551, Japan; patosanhueza@gmail.com
[2] National Astronomical Observatory of Japan, National Institutes of Natural Sciences, 2-21-1 Osawa, Mitaka, Tokyo 181-8588, Japan
[3] Department of Astronomical Science, SOKENDAI (The Graduate University for Advanced Studies), 2-21-1 Osawa, Mitaka, Tokyo 181-8588, Japan
[4] Department of Astronomy, Graduate School of Science, The University of Tokyo, 7-3-1 Hongo, Bunkyo-ku, Tokyo 113-0033, Japan
[5] Institut de Ciències de l'Espai (ICE, CSIC), Can Magrans s/n, 08193, Cerdanyola del Vallés, Catalonia, Spain
[6] Institut d'Estudis Espacials de Catalunya (IEEC), 08034, Barcelona, Catalonia, Spain
[7] Center for Astrophysics |Harvard & Smithsonian, 60 Garden Street, Cambridge, MA 02138, USA
[8] Department of Earth, Environment, and Physics, Worcester State University, Worcester, MA 01602, USA
[9] Green Bank Observatory, 155 Observatory Road, Green Bank, WV 24944, USA
[10] Joint ALMA Observatory, Alonso de Córdova 3107, Vitacura, Santiago, Chile
[11] National Radio Astronomy Observatory, 520 Edgemont Road, Charlottesville, VA 22903, USA
[12] Academia Sinica, Institute of Astronomy and Astrophysics, No.1, Sec. 4, Roosevelt Road, Taipei 10617, Taiwan
[13] SUPA, School of Physics and Astronomy, University of St. Andrews, North Haugh, St. Andrews, KY16 9SS, UK
[14] Max Planck Institute for Astronomy, Königstuhl 17, 69117 Heidelberg, Germany
[15] Shanghai Astronomical Observatory, Chinese Academy of Sciences, 80 Nandan Road, Shanghai 200030, People's Republic of China
[16] INAF-Osservatorio Astrofisico di Arcetri, Largo E. Fermi 5, I-50125 Firenze, Italy
[17] Yukawa Institute for Theoretical Physics, Kyoto University, Kyoto 606-8502, Japan
[18] Institute of Astronomy and Department of Physics, National Tsing Hua University, Hsinchu 300044, Taiwan
[19] Korea Astronomy and Space Science Institute (KASI), 776 Daedeokdae-ro, Yuseong-gu, Daejeon 34055, Republic of Korea
[20] Department of Physics and Astronomy, University College London, Gower Street, London, WC1E 6BT, UK
[21] Instituto Argentino de Radioastronomía (CCT- La Plata, CONICET, CICPBA, UNLP), C.C. No. 5, 1894, Villa Elisa, Buenos Aires, Argentina
[22] Department of Astronomy, University of Florida, P.O. Box 112055, Gainesville, FL 32611, USA
[23] Department of Physics, Indian Institute of Science Education and Research (IISER) Tirupati, Yerpedu, Tirupati - 517619, Andhra Pradesh, India
[24] School of Astronomy and Space Sciences, University of Chinese Academy of Sciences, No. 19A Yuquan Road, Beijing 100049, People's Republic of China
[25] Key Laboratory of Radio Astronomy and Technology, Chinese Academy of Sciences, A20 Datun Road, Chaoyang District, Beijing 100101, People's Republic of China
[26] East Asian Observatory, 660 N. A'ohōkū Place, University Park, Hilo, HI 96720, USA
[27] Univ. Lyon, Ens de Lyon, Univ. Lyon 1, CNRS, Centre de Recherche Astrophysique de Lyon UMR5574, 69007, Lyon, France
[28] School of Astronomy and Space Science, Nanjing University, 163 Xianlin Avenue, Nanjing 210023, People's Republic of China
[29] Key Laboratory of Modern Astronomy and Astrophysics, Nanjing University, Ministry of Education, Nanjing 210023, People's Republic of China
[30] Kavli Institute for Astronomy and Astrophysics, Peking University, Beijing 100871, People's Republic of China
[31] I. Physikalisches Institut, Universitt zu Köln, Zülpicher Str. 77, D-50937 Kln, Germany
[32] Department of Astronomy, School of Physics, Peking University, Beijing 100871, People's Republic of China
[33] Instituto de Radioastronomía y Astrofísica, Universidad Nacional Autónoma de México, P.O. Box 3-72, 58090, Morelia, Michoacán, México
[34] Graduate School of Informatics and Engineering, The University of Electro-Communications, Chofu, Tokyo 182-8585, Japan

Abstract

A complete understanding of the initial conditions of high-mass star formation and what processes determine multiplicity requires the study of the magnetic field in young massive cores. Using Atacama Large Millimeter/ submillimeter Array (ALMA) 250 GHz polarization observations ($0\rlap{.}''3 = 1000$ au) and ALMA 220 GHz high-angular-resolution observations ($0\rlap{.}''05 = 160$ au), we have performed a full energy analysis including the magnetic field at core scales and have assessed what influences the multiplicity inside a massive core previously believed to be in the prestellar phase. With a mass of 31 $M_\odot$, the G11.92 MM2 core has a young CS molecular outflow with a dynamical timescale of a few thousand years. At high resolution, the MM2 core fragments into a binary system, with a projected separation of 505 au and a binary mass ratio of 1.14. Using the Davis–Chandrasekhar–Fermi method with an angle dispersion function analysis, we estimate in this core a magnetic field strength of 6.2 mG and

[35] Corresponding author.

a mass-to-magnetic-flux ratio of 18. The MM2 core is strongly subvirialized, with a virial parameter of 0.064, including the magnetic field. The high mass-to-magnetic-flux ratio and low virial parameter indicate that this massive core is very likely undergoing runaway collapse, which is in direct contradiction with the core accretion model. The MM2 core is embedded in a filament that has a velocity gradient consistent with infall. In line with clump-fed scenarios, the core can grow in mass at a rate of $1.9–5.6 \times 10^{-4} \, M_\odot \, \mathrm{yr}^{-1}$. In spite of the magnetic field having only a minor contribution to the total energy budget at core scales (a few thousands of astronomical units), it likely plays a more important role at smaller scales (a few hundreds of astronomical units) by setting the binary properties. Considering energy ratios and a fragmentation criterion at the core scale, the binary system could have been formed by core fragmentation. The binary system properties (projected separation and mass ratio), however, are also consistent with radiation-magnetohydrodynamic simulations with super-Alfvenic or supersonic (or sonic) turbulence that form binaries by disk fragmentation.

Unified Astronomy Thesaurus concepts: Dust continuum emission (412); Polarimetry (1278); Star formation (1569); Star forming regions (1565); Massive stars (732); Magnetic fields (994); Young stellar objects (1834); Binary stars (154)

1. Introduction

How high-mass cores gather the necessary mass to form high-mass stars is still uncertain. Were they slowly formed under virial equilibrium conditions with most of their mass already in place early on, in a high-mass prestellar core? Or did they start with low mass under subvirial conditions?

The search for high-mass prestellar cores has been intense (Q. Zhang et al. 2009; P. Sanhueza et al. 2013, 2017, 2019; J. C. Tan et al. 2013; K. Wang et al. 2014; S. Ohashi et al. 2016; Y. Contreras et al. 2018; S. Li et al. 2019; T. Pillai et al. 2019; K. Morii et al. 2021, 2025; E. Redaelli et al. 2022), resulting in no detections at the early evolutionary stages found in infrared dark clouds (IRDCs; J. M. Rathborne et al. 2006; E. T. Chambers et al. 2009; P. Sanhueza et al. 2012). Among the recent studies of 70 μm dark IRDCs, the ALMA Survey of 70 μm Dark High-mass Clumps in Early Stages (the ASHES survey; P. Sanhueza et al. 2019) shows a complete absence of high-mass prestellar cores ($>30 \, M_\odot$) in 39 massive clumps containing 839 cores (K. Morii et al. 2023, 2024). The core dynamics analysis of the ASHES pilot survey (S. Li et al. 2023) shows that at larger masses, both prestellar and protostellar cores are more subvirialized, i.e., have lower virial parameters ($\alpha = M_{\mathrm{vir}}/M < 1$, with M_{vir} being the virial mass and M the total gas mass). Considering only turbulence and gravity, more massive cores are farther out of equilibrium and likely to collapse fast, unless there are other energies at play that could counter gravity, such as the magnetic field and rotation. Indeed, using ALMA, the magnetic field has been mapped in IRDC G28.34+0.06 (J. Liu et al. 2020) and IRDC 18310-4 (H. Beuther et al. 2018; K. Morii et al. 2021), with the finding that cores can have larger virial parameters after including the magnetic field but the most massive cores remain subvirial.

The rare high-mass prestellar core candidates found so far tend to be embedded in clumps more evolved than 70 μm dark IRDCs (e.g., J. C. Tan et al. 2013; C. J. Cyganowski et al. 2014; T. Liu et al. 2017; T. Nony et al. 2018; A. T. Barnes et al. 2023; X. Mai et al. 2024). Thorough analysis of their kinematics, physical, and/or chemical properties, however, found consistency with protostellar activity (e.g., S. Feng et al. 2016; J. C. Tan et al. 2016; J. Molet et al. 2019; C. J. Cyganowski et al. 2022). Nevertheless, the high-mass cores previously believed to be in the prestellar phase offer the opportunity to study a high-mass core at the onset of star formation.

In this regard, the massive core G11.92 MM2, with a mass $>30 \, M_\odot$ (C. J. Cyganowski et al. 2014), is sufficiently bright to be observed in millimeter/submillimeter polarization, allowing the study of the magnetic field and its importance in the star formation process. Because the evidence of star formation in G11.92 MM2 suggests that it is very young, the energy balance and virial equilibrium analysis in this young protostellar core can be used as a proxy to infer which physical conditions were present in the prestellar phase. Another key aspect for which the study of a young core is of great advantage is for determining which physical processes influence multiplicity. The fragmentation of cores and/or accretion disks is regulated not only by gravity and thermal pressure, but also by turbulence and magnetic fields that can introduce asymmetries and rotation, promoting the formation of multiple systems (S. S. R. Offner et al. 2023). On this point, the recently discovered binary system in G11.92 MM2 (C. J. Cyganowski et al. 2022) offers the possibility of studying which physical conditions caused the fragmentation.

The G11.92 region, located at a distance of 3.37 kpc (M. Sato et al. 2014), is forming a young stellar cluster (C. J. Cyganowski et al. 2017). The brightest object in the region is MM1, a high-mass star of $\sim 1.2 \times 10^4 \, L_\odot$ (L. Moscadelli et al. 2016) forming through an accretion disk (J. D. Ilee et al. 2016, 2018). While the MM2 core eluded the detection of signs indicating active star formation for almost a decade, the finding of an embedded protobinary system with 1.3 mm brightness temperatures indicative of internal heating and a low-velocity molecular outflow in CH_3OH emission reveals star formation activity at 100 au scales. More recently, S. Zhang et al. (2024) have shown that the MM2 core is actively accreting mass from its large-scale environment. C. J. Cyganowski et al. (2022) suggest that the binary may be forming in a weakly magnetized environment, which could be confirmed by full-polarization observations that could unveil the local magnetic field.

In the Magnetic fields in Massive star-forming Regions (MagMaR) project, we have observed 30 high-mass star-forming regions in polarization at 1.2 mm ($\sim 250 \, \mathrm{GHz}$) using ALMA. The first papers describing the results from this project show a variety of magnetic field morphologies: radially oriented due to an explosive event (M. Fernández-López et al. 2021); hourglass-like, implying a strong field (P. C. Cortes et al. 2021; P. Saha et al. 2024); spiral-shaped, indicating a gravity-dominated system (P. Sanhueza et al. 2021; P. C. Cortes et al. 2024); and aligned with velocity gradients that likely trace material flowing toward a high-mass star (L. A. Zapata et al. 2024). As part of MagMaR, we have observed the G11.92 high-mass star-forming region, including the aforementioned former high-mass prestellar core

MM2. While the MagMaR project offers the mapping of the magnetic field at core scales, the Digging into the Interior of Hot Cores with ALMA (DIHCA) survey provides a view on how the cores embedded in the same 30 fields fragment at scales of a few hundred astronomical units using ALMA at 220 GHz (F. A. Olguin et al. 2022, 2023; K. Taniguchi et al. 2023; K. Ishihara et al. 2024; S. Li et al. 2024).

In this paper, we combine observations of G11.92 MM2 from the MagMaR and DIHCA surveys to measure the core-scale magnetic field and constrain the importance of the magnetic fields at the earliest stages of massive binary formation.

2. Observations

2.1. Polarization Observations

Full-polarization observations were taken as part of the MagMaR survey (Project IDs: 2017.1.00101.S and 2018.1.00105.S; PI: Sanhueza). Observations at 1.2 mm (~250.486 GHz) of G11.92-0.61 were carried out on 2018 September 25, using 47 antennas of the 12 m array. An angular resolution of ~$0\farcs3$ (~1000 au) was obtained, with unprojected baselines ranging from 15 to 1400 m. The correlator setup included five spectral windows: two spectral windows of 234 MHz width, providing a spectral resolution of 0.488 MHz (0.56 km s^{-1}), and three spectral windows of 1875 MHz width, with a spectral resolution of 1.95 MHz (2.4 km s^{-1}). The data calibration and imaging were performed using CASA versions 5.1.1 and 5.5.0, respectively.

We adopted the procedures described in F. A. Olguin et al. (2021) to remove channels with line emission from the continuum (Stokes I) image. Stokes I was self-calibrated in phase and amplitude. Self-calibration solutions were also applied to the spectral cubes.

Each Stokes parameter image was independently cleaned using the CASA task *tclean*, with Briggs weighting and a robust parameter equal to 1. The final images have an angular resolution of $0\farcs27 \times 0\farcs34$ and sensitivities of 181 μJy beam^{-1} for Stokes I (σ_I) and 30.3 μJy beam^{-1} for both Stokes Q and U (σ_{QU}). The polarized intensity image was debiased following J. E. Vaillancourt (2006).

The automatic masking procedure *yclean* presented in Y. Contreras et al. (2018) was used for the imaging of the line emission. The CASA task *tclean* with Briggs weighting and a robust parameter equal to 1 was used, producing a noise level of 1.3 mJy beam^{-1} per ~2.4 km s^{-1} channel for CS $J = 5 - 4$ and CH$_3$CN ($v = 0$, $J = 14 - 13$) and 3.0 mJy beam^{-1} per 0.56 km s^{-1} channel for H^{13}CO$^+$ $J = 3 - 2$.

2.2. High-resolution Observations

Long-baseline observations were taken as part of the DIHCA survey (Project IDs: 2016.1.01036.S and 2017.1.00237.S; PI: Sanhueza). Observations at 1.33 mm (~226.2 GHz) of G11.92-0.61 were carried out on 2017 September 11 and 2019 July 28, using 42 antennas of the 12 m array. An angular resolution of ~$0\farcs048$ (~160 au) was obtained, with unprojected baselines ranging from 42 to 8548 m. The correlator setup included four spectral windows of 1875 MHz width and a spectral resolution of 976 kHz (~1.3 km s^{-1}). Data calibration and imaging were performed using CASA versions 5.6.1-8 and 5.7.0, respectively.

As for the polarization data, we also remove channels with line emission from the continuum via the procedure in F. A. Olguin et al. (2021). In the DIHCA data, a large number of molecular lines have been detected in the core MM1 of G11.92, but none have been detected in the core MM2. Continuum emission was self-calibrated in phase and amplitude. The continuum emission was cleaned using the CASA task *tclean*, with Briggs weighting and a robust parameter equal to 0.5. The final images have an angular resolution of $0\farcs055 \times 0\farcs042$ and sensitivity of 36.1 μJy beam^{-1}.

3. Results

Figure 1(a) shows the 1.2 mm dust continuum emission image (and white contours) with the magnetic field directions projected onto the plane of the sky in green segments at 1000 au scales. The centrally condensed MM2 core has dust emission extending to the northern and western parts that are followed by the magnetic field. At the center of the MM2 core, the 1.3 mm high-angular-resolution data (160 au resolution, in black contours) from the DIHCA survey show the fragmentation of the MM2 core into a binary system (MM2-E and MM2-W; C. J. Cyganowski et al. 2022).

So far, there has been no successful detection of compact molecular line emission emanating from the center of the MM2 core. In Figure 1(b), we show compact CH$_3$CN ($v = 0$, $J = 14 - 13$) emission (the moment 0 map of the $K = 0$ and $K = 1$ transitions combined, E_u/κ_B being equal to 92.7 and 99.8 K, respectively) coming from what seems to be a common compact structure hosting MM2-E and MM2-W. The detection of these transitions with $E_u/\kappa_B > 90$ K implies internal heating and deeply embedded star formation activity. Figure 1(b) also shows a molecular outflow in CS ($J = 5 - 4$). Considering the spatial resolution of 1000 au of the CS emission, it is unclear which of the binary members drives the outflow.

Using the CS outflow emission, the projected lengths of the blue- and redshifted lobes (l_b, l_r) are estimated to be 18,000 and 2500 au (blueshifted emission toward the southwest and redshifted emission toward the north), respectively, while the maximum velocities ($v_{maxb} = |v_{LSR}^b - v_{sys}|$ and $v_{max\,r} = |v_{LSR}^r - v_{sys}|$ with $v_{sys} = 37.1$ km s^{-1}) correspond to 19.1 and 8.4 km s^{-1}, respectively. These values result in outflow dynamical timescales ($t_{dyn} = l_{b,r}/v_{maxb,r}$) of 4500 yr for the blueshifted lobe and 1400 yr for the redshifted lobe, supporting the idea that the MM2 core has recently entered the protostellar stage and is at the onset of star formation.[36]

In addition to the compact and outflow emission, we also find in the H^{13}CO$^+$ ($J = 3 - 2$) emission a more extended gas component tracing the whole MM2 core and a larger filamentary structure connecting with the core from the north and south. Figure 2(a) shows the integrated intensity of the single component of H^{13}CO$^+$ emission that has a spatial distribution coincident with that of the dust emission. The H^{13}CO$^+$ profiles are Gaussian-like, except at the center of the core, near the position of the CH$_3$CN emission, where the line emission exhibits a profile with absorption features at the velocity of the G11.92 cloud, i.e., 35.2 km s^{-1} (T. Csengeri et al. 2016). Because the $J = 3 - 2$ transition presents a simple line profile and traces dense, relatively cold gas ($E_u/\kappa_B = 25$ K), it can

---

[36] The dynamical timescale has not been corrected by the unknown inclination of the outflow. S. Li et al. (2020) calculate that for a mean inclination angle of ~$57\fdg3$, a correction factor of 0.6 should be applied to t_{dyn}, resulting in dynamical ages of 2700 yr for the blueshifted lobe and 840 yr for the redshifted lobe.
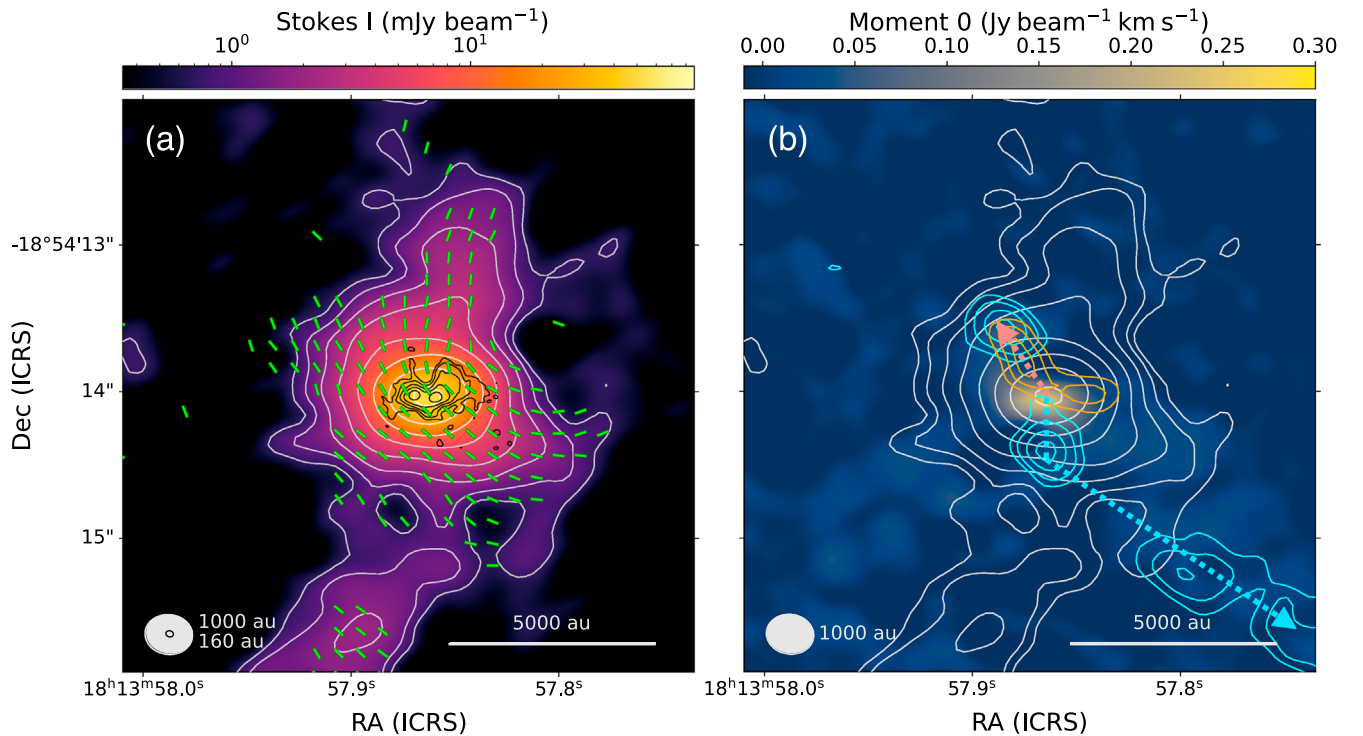
Figure 1. (a) ALMA 1.2 mm dust continuum emission (color scale and white contours) toward G11.92-0.61 MM2, with overlaid magnetic field segments. Green line segments representing the magnetic field orientation (dust polarization vectors rotated by 90°, plotted in Nyquist sampling) are plotted above the $3\sigma_{QU}$ level, with $\sigma_{QU} = 30~\mu$Jy beam^{-1}, and have an arbitrary length. The white contours correspond to the dust continuum emission at low resolution (~0″3) in steps of 4, 6, 10, 18, 34, 66, 130, and 258 times the σ_I (rms) value of 181 μJy beam^{-1}. The black contours correspond to the 1.33 mm dust continuum emission at high angular resolution (~0″05) in steps of 5, 10, 20, 40, and 80 times the sigma value of 36.1 μJy beam^{-1}. (b) Moment 0 map of the $K = 0$ and $K = 1$ transitions combined of CH$_3$CN ($v = 0$, $J = 14$–13) in color scale. The white contours represent the dust continuum emission, as in (a). The cyan and orange contours correspond to the blueshifted and redshifted outflow emission traced by CS $J = 5 - 4$ in steps of 3, 5, 8, and 11 times the sigma value of 10 mJy beam^{-1} km s^{-1} and in steps of 3, 4, 5, and 6 times the sigma value of 4.7 mJy beam^{-1} km s^{-1}, respectively. The blueshifted component is integrated from 18 to 32.9 km s^{-1} and the redshifted component from 41.3 to 44.9 km s^{-1}. The cyan and orange arrows represent the direction of the CH$_3$OH outflow detected by C. J. Cyganowski et al. (2022). The white and black beams at the bottom left represent the spatial resolution of the polarization observations at 1000 au (0″3) and the high-angular-resolution observations at 160 au (0″05), respectively. A scale bar is shown to the bottom right of each panel.

be used to extract the kinematics of the core, namely rotation and turbulence. We have performed a Gaussian fitting, pixel by pixel, and the results are presented in Figures 2(b) and (c). The masked pixels at the center of the core correspond to places at which the Gaussian fitting failed. The integrated intensity map (Figure 2(a)) shows weaker emission at the center of the core. We find no evidence of core rotation, meaning that the core, if rotating, could be doing so in or near the plane of the sky and/or the rotational velocity is small and unresolved at the current spectral resolution. This lack of rotation is not unusual at the early stages of high-mass star formation (see, e.g., the cores named W43-MM1#6 and G028.37+00.07 C2c1; A. T. Barnes et al. 2023; N. Cunningham et al. 2023), and it can even occur in more evolved hot cores (see, e.g., A. Silva et al. 2017; P. Saha et al. 2024). We do see, however, an overall velocity gradient in the filamentary structure that hosts the MM2 core, with a bluer component toward the north and a redder component toward the south (Figure 2(b)).

4. Discussion

4.1. MM2 Core Properties from Dust (Stokes I) and Line Emission

To measure the properties of the MM2 core, we use the dendrogram definition made for the whole MagMaR core catalog presented in P. Sanhueza et al. (2025, in preparation). The dendrogram leaf representing the core is shown in

Figure 2(a) (see Appendix A.1 for details of the dendrogram parameters). This leaf defines the area over which the velocity dispersion, magnetic field strength, and energies are later derived. The measured flux density and radius for the MM2 core at 1.2 mm are 163 mJy and 0″37 (corresponding to 1250 au), respectively. Assuming optically thin dust emission and a dust temperature of 20 K (C. J. Cyganowski et al. 2014), we obtain a mass and an average number density for the MM2 core of $31 \pm 13~M_\odot$ and $4.8 \pm 2.5 \times 10^8$ cm^{-3}, respectively (more details can be found in Appendix A.1).

The measured velocity width (FWHM) of the H^{13}CO$^+$ line in the leaf area defining MM2 is 1.44 km s^{-1}, corresponding to a Mach number ($\mathcal{M}$) of 2.3 (see the details in Appendix A.2). This value of $\mathcal{M}$ is consistent with the values found for the most massive cores embedded in IRDCs (S. Li et al. 2023).

Using the high-angular-resolution DIHCA data, we fitted a 2D Gaussian profile to each of both dust condensations to obtain their positions and fluxes. The projected separation between the two peak positions of 0″15 (505 au) is consistent with the one derived by C. J. Cyganowski et al. (2022). The flux densities at 1.33 mm are 14.88 mJy for MM2-E and 16.91 mJy for MM2-W. Assuming that both condensations have the same dust temperature, their mass ratio is 1.14.
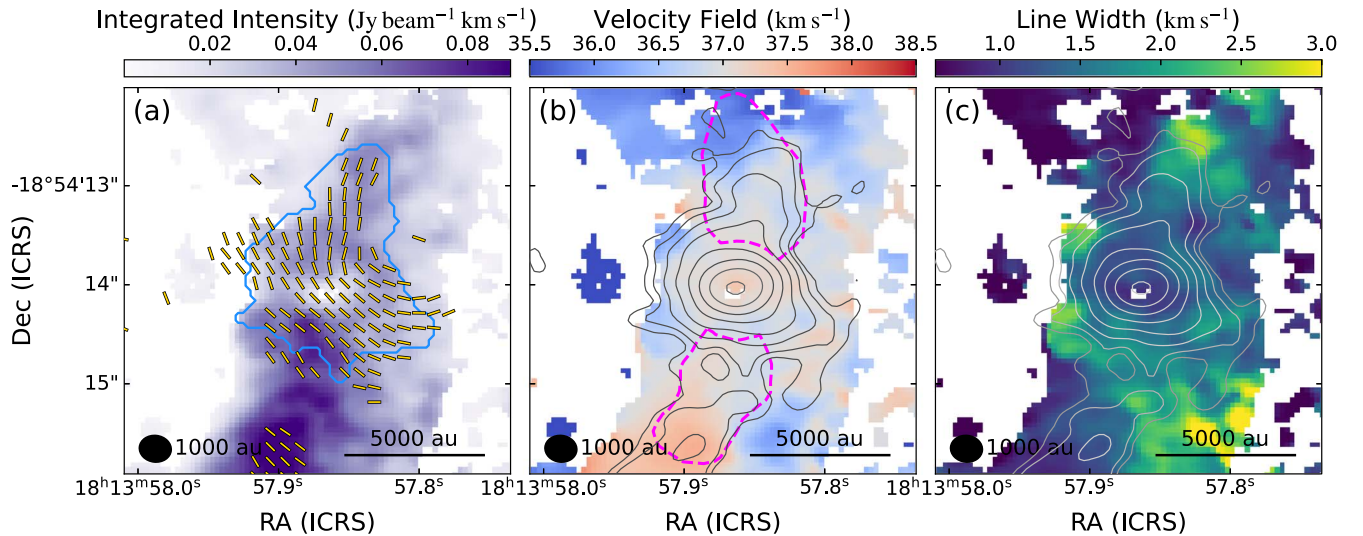
Figure 2. Integrated intensity (a), velocity field (b), and line FWHM (c) obtained from fitting a Gaussian component to the H^{13}CO$^+$ emission, pixel by pixel. The contours show the dust continuum emission (the same as in Figure 1). All pixels that have a peak intensity, as derived from the Gaussian fitting, larger than 4σ ($\sigma = 3$ mJy beam^{-1}) are displayed. In (a), the dendrogram leaf, defined from the continuum emission, is displayed in blue (see the details in Appendix A.1) and the magnetic field vectors in yellow. The core properties were measured inside the leaf. In (b), the areas used to derive the properties of the infalling gas are shown with the dashed magenta masks.

4.2. Mass Feeding

In recent years, it has become more frequent to find velocity gradients consistent with accretion flows (or streamers) in high-mass star-forming regions (e.g., N. Peretto et al. 2014; H. B. Liu et al. 2015; A. F. Izquierdo et al. 2018; H.-R. V. Chen et al. 2019; P. Sanhueza et al. 2021; M. Fernández-López et al. 2023; F. A. Olguin et al. 2023; F.-W. Xu et al. 2023; R. H. Álvarez-Gutiérrez et al. 2024; M. R. A. Wells et al. 2024). The velocity field of the H^{13}CO$^+$ emission (Figure 2(b)) shows how the northern gas becomes more blueshifted away from the core, while the southern gas becomes more redshifted away from the core. The v_{lsr} velocity around the MM2 core is $\sim$37.1 km s^{-1}. This pattern in the velocity gradient has previously been interpreted as flows of gas moving toward the center (e.g., H. Kirk et al. 2013; N. Peretto et al. 2014). We have fitted the velocity field inside an area approximately located at the 4σ contour in the continuum (see the exact region in Figure 2(b)). The velocity gradient (∇V_{obs}) was determined by using a linear regression applied to average projected velocities in bins of 0″.2 with respect to the central source, similar to a radial velocity profile inside the masked area. The derived velocity gradient is of 61.5 km s^{-1} pc^{-1} in the northern blueshifted component and 26.9 km s^{-1} pc^{-1} in the southern redshifted component (Figure 3). Using the dust continuum emission and assuming a dust temperature of 20 K, the gas mass in the same area where the velocity gradients were measured is 4.0 and 2.5 $M_\odot$ for the blueshifted and redshifted flows, respectively. Following H. Kirk et al. (2013) and using the measured ∇V_{obs}, we can estimate the infall rate as $\dot{M} = M \nabla V_{obs}/\tan(i)$, resulting in $\dot{M}_{blue} = 2.5 \times 10^{-4}/\tan(i)$ and $\dot{M}_{red} = 6.9 \times 10^{-5}/\tan(i) M_\odot$ yr^{-1}, with i being the inclination angle. We derive a total infall rate of 1.9–$5.6 \times 10^{-4} M_\odot$ yr^{-1} for arbitrary inclination angles between $60°$ and $30°$, respectively, consistent with the values derived in the region at larger scales using N$_2$H$^+$ emission by S. Zhang et al. (2024).
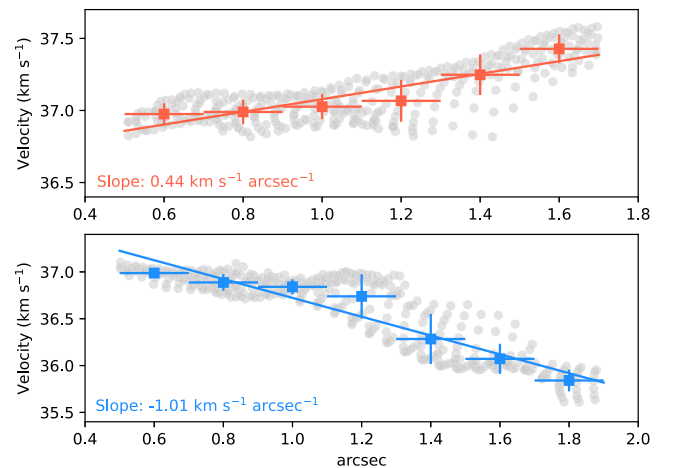

Figure 3. Fitted velocity field for deriving the velocity gradient in the filaments. The error bars correspond to the bin width and the standard deviation of the velocities inside each bin for the horizontal and vertical axes, respectively. In the top panel, the velocity gradient of 0.44 km s^{-1} arcsec^{-1} corresponds to 26.9 km s^{-1} pc^{-1}, while in the bottom panel, the velocity gradient of 1.01 km s^{-1} arcsec^{-1} corresponds to 61.5 km s^{-1} pc^{-1}.

4.3. The Magnetic Field and Energy Balance

To assess the importance of the magnetic field with respect to the other energies in play and to determine if the magnetic field has a role in the formation of the binary system, we estimate the magnetic field strength using the Davis–Chandrasekhar–Fermi (DCF) method (L. Davis 1951; S. Chandrasekhar & E. Fermi 1953), using the angle dispersion function (ADF) approach (M. Houde et al. 2009, 2016). As described in Appendix B, we estimate a magnetic field strength of 6.2 ± 3.5 mG, a mass-to-magnetic-flux ratio (λ) of 18 ± 9, and an Alfvenic Mach number ($\mathcal{M}_A$) of 1.6 ± 0.7. In spite of having a relatively large field strength, the core is unquestionably magnetically supercritical, even with the uncertainties given by the DCF technique (J. Liu et al. 2021). The magnetic field cannot prevent the collapse of the core.

In one of the scenarios that aims to explain the formation of high-mass stars, the core accretion theory, the virial equilibrium of high-mass cores is important to enable a "slow" collapse (i.e., over several freefall times; J. C. Tan et al. 2014). Due to the general difficulty in evaluating the magnetic field strength in star-forming regions, virial analyses are frequently performed neglecting the magnetic field (e.g., S. Li et al. 2023). Only considering the kinetic support, we calculate a virial parameter (α_{vir}) of 0.060 $\pm$ 0.026, far from equilibrium, $\alpha_{vir} = 1$ (Appendix A.2). However, as suggested in previous works (e.g., J. C. Tan et al. 2013; P. Sanhueza et al. 2017; J. Liu et al. 2022a), the magnetic field can add additional support to maintain a core in equilibrium. Following Appendix B, we find that the virial parameter including the magnetic energy ($\alpha_{vir,B}$) is 0.064 $\pm$ 0.028. This value is consistent with the kinetic virial parameter, within the uncertainties, and it is clearly insufficient to bring the MM2 core to equilibrium.

Lacking compact emission from Spitzer, the MM2 core was scrutinized for signs of star formation activity for many years, using several observational facilities (the Submillimeter Array, the Very Large Array, and ALMA; C. J. Cyganowski et al. 2014, 2017). MM2 was considered one of the most promising high-mass prestellar candidates until the discovery of a weak outflow in CH_3OH (C. J. Cyganowski et al. 2022), now also detected here in CS $J = 5 - 4$. Indeed, the presence of only weak, compact CH_3CN emission and an outflow dynamical timescale of only a few thousand years strongly suggest that the star formation must have been relatively recent. We can therefore adopt MM2 as a proxy to infer what the physical conditions were in the prestellar phase. Adopting the core accretion paradigm, we argue that, by extrapolating the core properties into the past prestellar phase, the virial parameter estimated at the current time is comparable or higher. First, the energies that can oppose collapse were likely weaker in the prestellar phase, because the core should have been less turbulent than at the present time (e.g., no injection of turbulence into the envelope from a protostar). Second, the magnetic field should have been weaker because of the lower gas density, on average. However, under the assumption of core accretion, the core mass should not have significantly changed, making the gravitational energy approximately the same as the current measured value. We therefore conclude that even with the inclusion of the magnetic field, high-mass stars cannot form in MM2 under equilibrium conditions. This conclusion stands in stark contradiction to the core accretion scenario.

Considering the environment in which MM2 is embedded, a filament with a velocity gradient consistent with a mass infall rate of a few times $10^{-4} M_\odot$ yr^{-1}, and a runaway collapse as indicated by the high mass-to-magnetic-flux ratio ($\lambda = 18 \pm 9$) and low virial parameter ($\alpha = 0.064 \pm 0.028$), clump-fed scenarios seem more likely.

Using numerical simulations, J. Liu et al. (2021) show that when the magnetic field is weak with respect to other energies, i.e., not in equipartition, the DCF with the ADF method overestimates the magnetic field strength. Therefore, the virial parameter including the magnetic field can be considered an upper limit. To consider the effect of the dust temperature on the core properties, we have calculated all core parameters at 50 K (see Tables 1 and 2 in Appendices A.2 and B, respectively).

With a $\alpha_{vir,B}$ equal to 0.23 $\pm$ 0.10 and $\lambda = 10 \pm 5$, all conclusions hold.

4.4. Magnetic Field and Binary Formation

With a separation in the plane of the sky of 505 au and a mass ratio of 1.14, the binary system in MM2 is likely one of the youngest observed among the few multiple systems known in high-mass star-forming regions (Y. Zhang et al. 2019; A. E. Guzmán et al. 2020; K. E. I. Tanaka et al. 2020; M. T. Beltrán et al. 2021; F. A. Olguin et al. 2022; S. Li et al. 2024). With the closest neighboring condensation at 2″9 (almost 10,000 au) away from the binary system (embedded in the MM5 core; C. J. Cyganowski et al. 2017), the binary system has likely been dynamically unperturbed and its properties should reflect the physical conditions near the moment of its formation.

T. Tsuribe & S.-i. Inutsuka (1999) formalized a criterion to assess whether a core is prone to fragmentation that depends on the ratio of the thermal to gravitational energy (α') and the ratio of the rotational to gravitational energy (β'). Fragmentation requires the following two conditions be met simultaneously: $\alpha'\beta' < 0.12$ and $\alpha' < 0.5$. For the MM2 core, we obtain $\alpha'\beta' = 8 \pm 7 \times 10^{-6}$ and $\alpha' = 5 \pm 2 \times 10^{-3}$ (see the details in Appendix A.2). The formalism derived by T. Tsuribe & S.-i. Inutsuka (1999), which ignores the magnetic field, indicates that the binary in the MM2 core can be formed through core fragmentation. Although not dominant, the presence of the magnetic field can nevertheless play against core fragmentation (B. Commerçon et al. 2011; A. T. Myers et al. 2013). M. N. Machida et al. (2008) find that for models having initial ratios of E_{rot}/E_G equal to 0.005, comparable to the values in the MM2 core (0.002–0.005 for 20–50 K), core fragmentation occurs for $\lambda > 10$ (consistent with the values in the MM2 core, λ of 10–18 for 20–50 K). The combination of absent/weak rotation at the core scale and the presence of a non-energetically-dominant magnetic field, along with an overall dominant gravitational energy, makes the formation of the binary system through core fragmentation viable in the MM2 core.

There are few simulations of cores that end with forming binaries including high-mass stars (e.g., M. R. Krumholz et al. 2009; R. Mignon-Risse et al. 2021, 2023). In radiation-hydrodynamical simulations, M. R. Krumholz et al. (2009) obtain a binary system formed by disk fragmentation with a mass ratio of 1.4 and a separation of 1590 au. R. Mignon-Risse et al. (2023) argue that the magnetic field can remove angular momentum in the innermost core regions, contributing to having smaller disks and smaller binary separations than hydrodynamical simulations suggest. R. Mignon-Risse et al. (2021) report the formation of binary systems from disk fragmentation, rather than core fragmentation, when turbulence dominates over the magnetic field (super-Alfvenic turbulence). This is in agreement with our observations of MM2, with an Alfvenic Mach number ($\mathcal{M}_A$) of 1.6 $\pm$ 0.7.

Among the available radiation-magnetohydrodynamical simulations of cores forming binary systems including high-mass stars, the so-called SUPAS simulation, run with super-Alfvenic, supersonic turbulence, from R. Mignon-Risse et al. (2021), results in the best match with the properties derived from our observations. Some of the conditions of the SUPAS simulation include a sonic Mach number ($\mathcal{M}$), an Alfvenic Mach number ($\mathcal{M}_A$), and a mass-to-magnetic-flux ratio

normalized to the critical value (λ) of 2, 5.7, and 5, respectively, while the measured values toward MM2 correspond to 2.30 ± 0.03, 1.6 ± 0.7, and 18 ± 9, respectively. However, the SUPA simulation with super-Alfvenic, sonic turbulence cannot be fully discarded, considering that the turbulence in the prestellar phase could have been lower ($\mathcal{M} = 0.5$, $\mathcal{M}_A = 1.4$, $\lambda = 5$). There are differences between the observations and the simulation conditions, however. For example, the magnetic field seems to be less important with respect to turbulence for the SUPAS simulation ($\mathcal{M}_A = 5.7$) and comparable for the SUPA simulation ($\mathcal{M}_A = 1.4$), but the magnetic field is more important with respect to gravity in both simulations ($\lambda = 5$). In spite of the differences, the obtained binary system formed through disk fragmentation has mass ratios between 1.1 and 1.6 and separations that range from 400 to 700 au for SUPAS and 350 to 600 au for SUPA, in good agreement with the observations.

Whether the binary system embedded in MM2 formed through core fragmentation or disk fragmentation, the magnetic field likely influences the fragmentation process at scales of a few hundred astronomical units. In the case of core fragmentation, it may reduce the number of fragments, while in disk fragmentation, it could determine the binary's properties, such as the mass ratio and separation. Now that observations offer important constraints to theoretical models, numerical simulations with clear, testable predictions are essential for distinguishing between these two fragmentation modes.

5. Conclusions

Studies including a complete energy analysis at the earliest stages of high-mass star formation are rare, especially at $\leqslant 1000$ au scales. Numerical simulations have tackled the origin of multiplicity by exploring the influence of different physical processes. Observations to test the validity of the resulting theoretical simulations are frequently difficult to obtain—for example, polarization and long baseline interferometric observations. Combining the MagMaR and the DIHCA surveys, we have analyzed the magnetic field and fragmentation of a young high-mass core (G11.92 MM2). We summarize our findings as follows:

1. In spite of having a relatively strong magnetic field of 6.2 ± 3.5 mG, the combined effect of turbulence and the magnetic field cannot oppose the gravitational collapse of the core (virial parameter of 0.064 ± 0.028 and mass-to-magnetic-flux ratio of 18 ± 9). In addition to being subvirialized and magnetically supercritical, the MM2 core is being fed with gas from its host filament at a rate of 1.9–5.6 $\times$ $10^{-4} M_{\odot}$ yr^{-1}. Considering that the MM2 core is very young and can be used as a proxy for the properties that the core had when it was prestellar, the formation scenario drawn in these observations contradicts the core accretion model and supports clump-fed scenarios.

2. Despite having only a minor contribution to the total energy budget at 1000 au scales (core scales), the magnetic field seems to be more important at scales of a few hundred astronomical units, influencing the fragmentation of MM2 and possibly shaping the properties of the binary system. Based on the analysis of energy ratios and a fragmentation criterion proposed from numerical simulations, the MM2 core could fragment following core fragmentation, but this

fragmentation should be limited. Comparing the binary properties (mass ratio of 1.14 and separation of 505 au) and the MM2 core properties ($\mathcal{M}$ of 2.30 ± 0.03, $\mathcal{M}_A$ of 1.6 ± 0.7, and λ of 18 ± 9) with radiation-magnetohydrodynamical simulations, we conclude that we cannot rule out the binary system possibly being formed by disk fragmentation under the influence of super-Alfvenic or supersonic (or sonic) turbulence.

Appendix A
Core Properties Excluding the Magnetic Field

A.1. Properties from Dust Continuum Emission

P. Sanhueza et al. (2025, in preparation) apply the dendrogram technique implemented in the Astrodendro Python package[37] (E. W. Rosolowsky et al. 2008) to define the core properties. The input parameters used for the dendrogram are 5σ as the minimum threshold for a leaf (core) detection and 1σ as the minimum significance for separating leaves, with the minimum size for the definition of a leaf being the number of pixels equal to those contained in half of the synthesized beam. Among the many outputs from Astrodendro, we obtain a flux density (primary-beam-corrected) of 163 mJy and a radius (R) defined as half the geometric mean of the FWHM of $0\farcs37$ (1250 au) at 1.2 mm wavelength.

The total gas mass is calculated from the dust continuum, assuming optically thin emission, as

$$M = \mathbb{R}\ \frac{F_\nu D^2}{\kappa_\nu B_\nu(T)}, \tag{A1}$$

where $\mathbb{R}$ is the gas-to-dust mass ratio, F_ν is the source flux density, D is the distance to the source, κ_ν is the dust opacity per gram of dust, and B_ν is the Planck function at the dust temperature T. Assuming a gas-to-dust mass ratio of 100, a dust opacity of $1.03\ \mathrm{cm^2\,g^{-1}}$ (interpolated to 1.2 mm, assuming $\beta = 1.6$; V. Ossenkopf & T. Henning 1994), and a temperature of 20 K (C. J. Cyganowski et al. 2014), we calculate a total mass of $31 \pm 13\ M_\odot$. C. J. Cyganowski et al. (2014) derive a dust temperature between 17 and 19 K for the MM2 core using the (sub)millimeter spectral energy distribution, and we adopt here an upper limit of 20 K. The uncertainty in the mass is dominated by the uncertainty from the gas-to-dust mass ratio and the dust opacity, with 23% and 28% being the respective values (P. Sanhueza et al. 2017). The uncertainty for both the ALMA band 6 flux[38] and the parallax distance is on the order of 10% (M. Sato et al. 2014). The number density, defined as $n(\mathrm{H_2}) = M/$ (Volume $\times\ \mu_{\mathrm{H_2}} m_\mathrm{H}$), with $\mu_{\mathrm{H_2}}$ being the molecular weight per hydrogen molecule and m_H the hydrogen mass, is calculated assuming a spherical core of radius 1250 au. Assuming $\mu_{\mathrm{H_2}} = 2.8$, we obtain an $n(\mathrm{H_2})$ of $4.8 \pm 2.5 \times 10^8\ \mathrm{cm^{-3}}$.

To estimate the accretion flows, the mass was calculated following the prescription above, assuming a dust temperature of 20 K. The flux for the blueshifted and redshifted flows is 21.5 and 13.3 mJy, resulting in 4.0 and 2.5 $M_\odot$, respectively.

A.2. Dynamics and Energetics

The observed line width at the FWHM of the $\mathrm{H^{13}CO^+}$ ($V_{\mathrm{H^{13}CO^+}}$) averaged inside the MM2 core is $1.44 \pm 0.02\ \mathrm{km\,s^{-1}}$, which results in a velocity dispersion $\sigma_{\mathrm{H}}^{13}\mathrm{CO^+}$ of $0.61 \pm 0.01\ \mathrm{km\,s^{-1}}$ ($V_{\mathrm{H^{13}CO^+}} = 1.44\ \mathrm{km\,s^{-1}} = 2\sqrt{2\ln 2}\ \sigma_{\mathrm{H^{13}CO^+}}$).

The total gas velocity dispersion is given by $\sigma_{\mathrm{tot}} = \sqrt{\sigma_{\mathrm{th}}^2 + \sigma_{\mathrm{nt}}^2}$, in which the thermal velocity dispersion

---

(σ_{th}) and the nonthermal velocity dispersion (σ_{nt}) are

$$\sigma_{\mathrm{th}}^2 = \frac{k_\mathrm{B} T}{\mu_\mathrm{p} m_\mathrm{H}} \tag{A2}$$

and

$$\sigma_{\mathrm{nt}}^2 = \sigma_{\mathrm{H^{13}CO^+}} - \frac{k_\mathrm{B} T}{m_{\mathrm{H^{13}CO^+}}}, \tag{A3}$$

respectively. $\mu_\mathrm{p} = 2.33$ is the mean molecular weight per free particle considering H, He, and a negligible admixture of metals, and $m_{H^{13}CO^+}$ is the molecular mass of the $\mathrm{H^{13}CO^+}$ equal to $30\,m_\mathrm{H}$. Assuming that the nonthermal component is independent of the molecular tracer used, we can obtain σ_{tot} of $0.66 \pm 0.01\ \mathrm{km\,s^{-1}}$. The value of σ_{th} is $0.26\ \mathrm{km\,s^{-1}}$ at 20 K and the sonic Mach number ($\mathcal{M} = \sigma_{\mathrm{nt}}/\sigma_{\mathrm{th}} = 0.61/0.26$) is then 2.30 ± 0.03.

The dynamical state of the cores is generally assessed by using the virial theorem. The virial parameter (α_{vir}) is defined as the ratio between the virial mass (M_{vir}) and the total mass (typically determined from the dust continuum emission). A virial parameter of unity corresponds to equilibrium, $\alpha_{\mathrm{vir}} < 1$ implies gravitational collapse, and $\alpha_{\mathrm{vir}} > 1$ means the core will disperse. The most common virial analysis includes only gravity (E_G) and kinetic energy (E_K—turbulence and thermal energy, neglecting rotation):

$$E_\mathrm{G} = -\frac{GM^2}{R}\left(\frac{3-n}{5-2n}\right) \quad \text{and} \quad E_\mathrm{K} = \frac{3}{2} M \sigma_{\mathrm{tot}}^2. \tag{A4}$$

The virial parameter can be expressed as

$$\alpha_{\mathrm{vir}} = \frac{M_{\mathrm{vir}}}{M} = 3\left(\frac{5-2n}{3-n}\right)\frac{R \sigma_{\mathrm{tot}}^2}{GM}, \tag{A5}$$

resulting in $\alpha_{\mathrm{vir}} = 0.060 \pm 0.026$ for a centrally peaked density profile ($\rho(R) \propto R^{-n}$; $n = 2$), indicating that turbulence alone cannot provide enough support against gravitational collapse.

According to T. Tsuribe & S.-i. Inutsuka (1999), a core will fragment if the following two conditions are met: $\alpha'\beta' < 0.12$ and $\alpha' < 0.5$, in which $\alpha' (= E_{\mathrm{th}}/E_\mathrm{G})$ is the ratio of the thermal to gravitational energy and $\beta' (= E_{\mathrm{rot}}/E_\mathrm{G})$ is the ratio of the rotational to gravitational energy. To obtain the thermal energy (E_{th}), we replace σ_{tot} with σ_{th} on the right-hand side of Equation (A4). Following P. Sanhueza et al. (2021), the rotational energy (E_{rot}) is given by

$$E_{\mathrm{rot}} = \frac{1}{3} M v_{\mathrm{rot}}^2\left(\frac{3-n}{5-n}\right), \tag{A6}$$

in which v_{rot} is the rotational velocity. Because the core MM2 shows no clear rotation at the current spectral resolution, we adopt the spectral resolution as an upper limit for the rotation, i.e., $v_{\mathrm{rot}} = 0.56\ \mathrm{km\,s^{-1}}$. For the MM2 core, we obtain $\alpha'\beta' = 8 \pm 7 \times 10^{-6}$ and $\alpha' = 5 \pm 2 \times 10^{-3}$, indicating that the binary system could be formed by fragmentation at the core scale.

To assess whether the conclusions of this work are affected by the temperature adopted, we have also calculated the core properties assuming a dust temperature of 50 K. The values are compared with those obtained at 20 K in Table 1.

Table 1
Core Properties at Different Dust Temperatures Excluding the Magnetic Field

T (K)	M ($M_\odot$)	$n(H_2)$ (cm^{-3}) $\times 10^8$	σ_{th} (km s^{-1})	σ_{nt} (km s^{-1})	σ_{tot} (km s^{-1})	$\mathcal{M}$	E_G (erg) $\times 10^{46}$	E_K (erg) $\times 10^{44}$	E_{th} (erg) $\times 10^{43}$	E_{rot} (erg) $\times 10^{43}$	α_{vir}
20	31 ± 13	4.8 ± 2.5	0.26	0.61 ± 0.01	0.66 ± 0.01	2.30 ± 0.03	1.3 ± 1.1	4.0 ± 1.7	6.4 ± 2.7	2.1 ± 0.9	0.060 ± 0.026
50	10 ± 4	1.6 ± 0.8	0.42	0.60 ± 0.01	0.73 ± 0.01	1.44 ± 0.02	0.14 ± 0.12	1.6 ± 0.7	5.2 ± 2.2	0.7 ± 0.3	0.22 ± 0.10

Appendix B
Magnetic Field Properties

Following the procedure of J. Liu et al. (2024), we use the ADF method (M. Houde et al. 2016) to estimate the plane-of-sky total (ordered+turbulent) magnetic field strength as

$$B = 0.21\sqrt{4\pi\rho}\quad \sigma_v\left(\frac{\langle B_t^2\rangle}{\langle B^2\rangle}\right)^{-0.5},\qquad (B1)$$

where ρ is the gas density, σ_v is the turbulent velocity dispersion (assumed to be $\sigma_{nt}=0.61$ km s^{-1}), and $(\langle B_t^2\rangle/\langle B^2\rangle)^{0.5}$ is the turbulent-to-total magnetic field strength ratio, without correction for line-of-sight (LOS) integration. Because the ADF may not correctly account for the LOS signal integration in high-density regions, we additionally adopt a numerical correction factor of 0.21, to account for this effect (J. Liu et al. 2021). The turbulent-to-total field ratio $(\langle B_t^2\rangle/\langle B^2\rangle)^{0.5}$ is derived by fitting the ADF:

$$1 - \langle\cos[\Delta\Phi(l)]\rangle = a_2 l^2 + \frac{\langle B_t^2\rangle}{\langle B^2\rangle}C$$
$$\times\left\{\frac{1}{C_1}[1 - e^{-l^2/2(l_\delta^2 + 2l_{W1}^2)}]\right.$$
$$+ \frac{1}{C_2}[1 - e^{-l^2/2(l_\delta^2 + 2l_{W2}^2)}]$$
$$\left. - \frac{2}{C_{12}}[1 - e^{-l^2/2(l_\delta^2 + l_{W1}^2 + l_{W2}^2)}]\right\},\qquad (B2)$$

where $\Delta\Phi(l)$ is the angular difference of two position angles separated by l, l_{W1} is the ALMA beam size divided by $2\sqrt{2\ln 2}$, l_{W2} is the maximum recoverable scale of ALMA divided by $2\sqrt{2\ln 2}$, $a_2 l^2$ is the second-order term of the Taylor expansion for the ordered field, and l_δ is the turbulent correlation length. The coefficients are given by

$$C_1 = \frac{(l_\delta^2 + 2l_{W1}^2)}{\sqrt{2\pi}\,l_\delta^3},\qquad (B3)$$

$$C_2 = \frac{(l_\delta^2 + 2l_{W2}^2)}{\sqrt{2\pi}\,l_\delta^3},\qquad (B4)$$

$$C_{12} = \frac{(l_\delta^2 + l_{W1}^2 + l_{W2}^2)}{\sqrt{2\pi}\,l_\delta^3},\qquad (B5)$$

$$C = \left(\frac{1}{C_1} + \frac{1}{C_2} - \frac{2}{C_{12}}\right)^{-1}.\qquad (B6)$$

Note that our equations are slightly different from the original ones in M. Houde et al. (2016), because the effect of LOS signal integration is considered differently. By fitting the ADF of MM2 with approaches similar to J. Liu et al. (2020, 2024), we obtain $(\langle B_t^2\rangle/\langle B^2\rangle)^{0.5} = 0.43$, with a statistical uncertainty of 45% of its value when the numerical correction of 0.21 is used. The resulting plane-of-sky total magnetic field strength is $B = 5.0 \pm 2.8$ mG. Note that the energy equipartition assumption of DCF may not be satisfied and the LOS signal integration could be more significant in high-density regions (J. Liu et al. 2021), so the estimated field strength may only be an upper limit. Adopting the statistical relation $B_{3D} \sim B \times 1.25$ (J. Liu et al. 2022b), we obtain a 3D total field strength of $B_{3D} = 6.2 \pm 3.5$ mG. The Alfvén speed, given by $\sigma_A = B/\sqrt{4\pi\rho}$, is 0.37 ± 0.23 km s^{-1}, resulting in an Alfvenic Mach number ($=\sigma_{nt}/\sigma_A = 0.60/0.37$) of 1.6 ± 0.7.

The relative importance between the magnetic field and gravity is usually characterized by the normalized mass-to-magnetic-flux ratio (R. M. Crutcher et al. 2004). We calculate the normalized mass-to-magnetic-flux ratio as in J. Liu et al. (2022a):

$$\lambda = \frac{(M/\Phi_B)}{(M/\Phi_B)_{cr}} = 2\pi G^{1/2}\left[\frac{3}{2}\left(\frac{3-n}{5-2n}\right)\right]^{1/2}\frac{M}{\Phi_B},\qquad (B7)$$

where $\Phi_B = B\pi R^2$ is the magnetic flux. For $n = 2$, we obtain $\lambda = 18 \pm 9$, which suggests a magnetically supercritical state where gravity dominates the magnetic field.

The virial parameter considering support from both the turbulence and the magnetic field can be written as (J. Liu et al. 2024)

$$\alpha_{vir,B} = \frac{2E_K + E_B}{|E_G|},\qquad (B8)$$

where the magnetic energy (E_B) is given by

$$E_B = \frac{1}{8\pi}B^2 V = \frac{1}{6}B^2 R^3.\qquad (B9)$$

For MM2, we obtain $\alpha_{vir,B} = 0.064 \pm 0.028$, which is only slightly larger than the kinetic virial parameter ($\alpha_{vir} = 0.060 \pm 0.026$), but indistinguishable within the uncertainties. The small virial parameter indicates a dynamical collapsing state of MM2, far from equilibrium.

Table 2 shows the core properties including the magnetic field for a dust temperature of 50 K.

Table 2
Magnetic Field Properties at Different Dust Temperatures

T (K)	B_{3D} (mG)	σ_A (km s^{-1})	(cm^{-3})	λ (km s^{-1})	E_B (erg)	$\alpha_{vir,B}$
20	6.2 ± 3.5	0.37 ± 0.23	1.6 ± 0.7	18 ± 9	$4.2 \pm 4.1 \times 10^{43}$	0.064 ± 0.028
50	3.5 ± 2.0	0.37 ± 0.23	1.6 ± 0.7	10 ± 5	$1.4 \pm 1.3 \times 10^{43}$	0.23 ± 0.10

ORCID iDs

Patricio Sanhueza ⓘ https://orcid.org/0000-0002-7125-7685
Junhao Liu (刘峻豪) ⓘ https://orcid.org/0000-0002-4774-2998
Kaho Morii ⓘ https://orcid.org/0000-0002-6752-6061
Josep Miquel Girart ⓘ https://orcid.org/0000-0002-3829-5591
Qizhou Zhang ⓘ https://orcid.org/0000-0003-2384-6589
Ian W. Stephens ⓘ https://orcid.org/0000-0003-3017-4418
James M. Jackson ⓘ https://orcid.org/0000-0002-3466-6164
Paulo C. Cortés ⓘ https://orcid.org/0000-0002-3583-780X
Patrick M. Koch ⓘ https://orcid.org/0000-0003-2777-5861
Claudia J. Cyganowski ⓘ https://orcid.org/0000-0001-6725-1734
Piyali Saha ⓘ https://orcid.org/0000-0002-0028-1354
Henrik Beuther ⓘ https://orcid.org/0000-0002-1700-090X
Suinan Zhang (张遂楠) ⓘ https://orcid.org/0000-0002-8389-6695
Maria T. Beltrán ⓘ https://orcid.org/0000-0003-3315-5626
Yu Cheng ⓘ https://orcid.org/0000-0002-8691-4588
Fernando A. Olguin ⓘ https://orcid.org/0000-0002-8250-6827
Xing Lu (吕行) ⓘ https://orcid.org/0000-0003-2619-9305
Spandan Choudhury ⓘ https://orcid.org/0000-0002-7497-2713
Kate Pattle ⓘ https://orcid.org/0000-0002-8557-3582
Manuel Fernández-López ⓘ https://orcid.org/0000-0001-5811-0454
Jihye Hwang ⓘ https://orcid.org/0000-0001-7866-2686
Ji-hyun Kang ⓘ https://orcid.org/0000-0001-7379-6263
Janik Karoly ⓘ https://orcid.org/0000-0001-5996-3600
Adam Ginsburg ⓘ https://orcid.org/0000-0001-6431-9633
A.-Ran Lyo ⓘ https://orcid.org/0000-0002-9907-8427
Kotomi Taniguchi ⓘ https://orcid.org/0000-0003-4402-6475
Wenyu Jiao ⓘ https://orcid.org/0000-0001-9822-7817
Chakali Eswaraiah ⓘ https://orcid.org/0000-0003-4761-6139
Qiu-yi Luo (罗秋怡) ⓘ https://orcid.org/0000-0003-4506-3171
Jia-Wei Wang ⓘ https://orcid.org/0000-0002-6668-974X
Benoît Commerçon ⓘ https://orcid.org/0000-0003-2407-1025
Shanghuo Li ⓘ https://orcid.org/0000-0003-1275-5251
Fengwei Xu ⓘ https://orcid.org/0000-0001-5950-1932
Huei-Ru Vivien Chen ⓘ https://orcid.org/0000-0002-9774-1846
Luis A. Zapata ⓘ https://orcid.org/0000-0003-2343-7937
Eun Jung Chung ⓘ https://orcid.org/0000-0003-0014-1527
Fumitaka Nakamura ⓘ https://orcid.org/0009-0007-6357-6874
Sandhyarani Panigrahy ⓘ https://orcid.org/0000-0001-5431-2294
Takeshi Sakai ⓘ https://orcid.org/0000-0003-4521-7492

References

Álvarez-Gutiérrez, R. H., Stutz, A. M., Sandoval-Garrido, N., et al. 2024, A&A, 689, A74
Barnes, A. T., Liu, J., Zhang, Q., et al. 2023, A&A, 675, A53
Beltrán, M. T., Rivilla, V. M., Cesaroni, R., et al. 2021, A&A, 648, A100
Beuther, H., Soler, J. D., Vlemmings, W., et al. 2018, A&A, 614, A64
Chambers, E. T., Jackson, J. M., Rathborne, J. M., & Simon, R. 2009, ApJS, 181, 360
Chandrasekhar, S., & Fermi, E. 1953, ApJ, 118, 116
Chen, H.-R. V., Zhang, Q., Wright, M. C. H., et al. 2019, ApJ, 875, 24
Commerçon, B., Hennebelle, P., & Henning, T. 2011, ApJL, 742, L9
Contreras, Y., Sanhueza, P., Jackson, J. M., et al. 2018, ApJ, 861, 14
Cortés, P. C., Girart, J. M., Sanhueza, P., et al. 2024, ApJ, 972, 115

Cortés, P. C., Le Gouellec, V. J. M., Hull, C. L. H., et al. 2021, ApJ, 907, 94
Crutcher, R. M., Nutter, D. J., Ward-Thompson, D., & Kirk, J. M. 2004, ApJ, 600, 279
Csengeri, T., Leurini, S., Wyrowski, F., et al. 2016, A&A, 586, A149
Cunningham, N., Ginsburg, A., Galván-Madrid, R., et al. 2023, A&A, 678, A194
Cyganowski, C. J., Brogan, C. L., Hunter, T. R., et al. 2014, ApJL, 796, L2
Cyganowski, C. J., Brogan, C. L., Hunter, T. R., et al. 2017, MNRAS, 468, 3694
Cyganowski, C. J., Ilee, J. D., Brogan, C. L., et al. 2022, ApJL, 931, L31
Davis, L. 1951, PhRv, 81, 890
Feng, S., Beuther, H., Zhang, Q., et al. 2016, ApJ, 828, 100
Fernández-López, M., Girart, J. M., López-Vázquez, J. A., et al. 2023, ApJ, 956, 82
Fernández-López, M., Sanhueza, P., Zapata, L. A., et al. 2021, ApJ, 913, 29
Guzmán, A. E., Sanhueza, P., Zapata, L., Garay, G., & Rodrìguez, L. F. 2020, ApJ, 904, 77
Houde, M., Hull, C. L. H., Plambeck, R. L., Vaillancourt, J. E., & Hildebrand, R. H. 2016, ApJ, 820, 38
Houde, M., Vaillancourt, J. E., Hildebrand, R. H., Chitsazzadeh, S., & Kirby, L. 2009, ApJ, 706, 1504
Ilee, J. D., Cyganowski, C. J., Brogan, C. L., et al. 2018, ApJL, 869, L24
Ilee, J. D., Cyganowski, C. J., Nazari, P., et al. 2016, MNRAS, 462, 4386
Ishihara, K., Sanhueza, P., Nakamura, F., et al. 2024, ApJ, 974, 95
Izquierdo, A. F., Galván-Madrid, R., Maud, L. T., et al. 2018, MNRAS, 478, 2505
Kirk, H., Myers, P. C., Bourke, T. L., et al. 2013, ApJ, 766, 115
Krumholz, M. R., Klein, R. I., McKee, C. F., Offner, S. S. R., & Cunningham, A. J. 2009, Sci, 323, 754
Li, S., Sanhueza, P., Beuther, H., et al. 2024, NatAs, 8, 472
Li, S., Sanhueza, P., Zhang, Q., et al. 2020, ApJ, 903, 119
Li, S., Sanhueza, P., Zhang, Q., et al. 2023, ApJ, 949, 109
Li, S., Zhang, Q., Pillai, T., et al. 2019, ApJ, 886, 130
Liu, H. B., Galván-Madrid, R., Jiménez-Serra, I., et al. 2015, ApJ, 804, 37
Liu, J., Qiu, K., & Zhang, Q. 2022a, ApJ, 925, 30
Liu, J., Zhang, Q., Commerçon, B., et al. 2021, ApJ, 919, 79
Liu, J., Zhang, Q., Lin, Y., et al. 2024, ApJ, 966, 120
Liu, J., Zhang, Q., & Qiu, K. 2022b, FrASS, 9, 943556
Liu, J., Zhang, Q., Qiu, K., et al. 2020, ApJ, 895, 142
Liu, T., Lacy, J., Li, P. S., et al. 2017, ApJ, 849, 25
Machida, M. N., Tomisaka, K., Matsumoto, T., & Inutsuka, S.-i. 2008, ApJ, 677, 327
Mai, X., Liu, T., Liu, X., et al. 2024, ApJL, 961, L35
McMullin, J. P., Waters, B., Schiebel, D., Young, W., & Golap, K. 2007, in ASP Conf. Ser. 376, Astronomical Data Analysis Software and Systems XVI, ed. R. A. Shaw, F. Hill, & D. J. Bell (San Francisco, CA: ASP), 127
Mignon-Risse, R., González, M., & Commerçon, B. 2023, A&A, 673, A134
Mignon-Risse, R., González, M., Commerçon, B., & Rosdahl, J. 2021, A&A, 652, A69
Molet, J., Brouillet, N., Nony, T., et al. 2019, A&A, 626, A132
Morii, K., Sanhueza, P., Csengeri, T., et al. 2025, ApJ, in press
Morii, K., Sanhueza, P., Nakamura, F., et al. 2021, ApJ, 923, 147
Morii, K., Sanhueza, P., Nakamura, F., et al. 2023, ApJ, 950, 148
Morii, K., Sanhueza, P., Zhang, Q., et al. 2024, ApJ, 966, 171
Moscadelli, L., Sánchez-Monge, Á., Goddi, C., et al. 2016, A&A, 585, A71
Myers, A. T., McKee, C. F., Cunningham, A. J., Klein, R. I., & Krumholz, M. R. 2013, ApJ, 766, 97
Nony, T., Louvet, F., Motte, F., et al. 2018, A&A, 618, L5
Offner, S. S. R., Moe, M., Kratter, K. M., et al. 2023, in ASP Conf. Ser. 534, Protostars and Planets VII, ed. S. Inutsuka et al. (San Francisco, CA: ASP), 275
Ohashi, S., Sanhueza, P., Chen, H.-R. V., et al. 2016, ApJ, 833, 209
Olguin, F. A., Sanhueza, P., Chen, H.-R. V., et al. 2023, ApJL, 959, L31
Olguin, F. A., Sanhueza, P., Ginsburg, A., et al. 2022, ApJ, 929, 68
Olguin, F. A., Sanhueza, P., Guzmán, A. E., et al. 2021, ApJ, 909, 199
Ossenkopf, V., & Henning, T. 1994, A&A, 291, 943
Peretto, N., Fuller, G. A., André, P., et al. 2014, A&A, 561, A83
Pillai, T., Kauffmann, J., Zhang, Q., et al. 2019, A&A, 622, A54
Rathborne, J. M., Jackson, J. M., & Simon, R. 2006, ApJ, 641, 389
Redaelli, E., Bovino, S., Sanhueza, P., et al. 2022, ApJ, 936, 169
Rosolowsky, E. W., Pineda, J. E., Kauffmann, J., & Goodman, A. A. 2008, ApJ, 679, 1338
Saha, P., Sanhueza, P., Padovani, M., et al. 2024, ApJL, 972, L6
Sanhueza, P., Contreras, Y., Wu, B., et al. 2019, ApJ, 886, 102
Sanhueza, P., Girart, J. M., Padovani, M., et al. 2021, ApJL, 915, L10
Sanhueza, P., Jackson, J. M., Foster, J. B., et al. 2012, ApJ, 756, 60

Sanhueza et al.

Sanhueza, P., Jackson, J. M., Foster, J. B., et al. 2013, ApJ, 773, 123
Sanhueza, P., Jackson, J. M., Zhang, Q., et al. 2017, ApJ, 841, 97
Sato, M., Wu, Y. W., Immer, K., et al. 2014, ApJ, 793, 72
Silva, A., Zhang, Q., Sanhueza, P., et al. 2017, ApJ, 847, 87
Tan, J. C., Beltrán, M. T., Caselli, P., et al. 2014, in Protostars and Planets VI,
    ed. H. Beuther (Tucson, AZ: Univ. Arizona Press), 149
Tan, J. C., Kong, S., Butler, M. J., Caselli, P., & Fontani, F. 2013, ApJ, 779, 96
Tan, J. C., Kong, S., Zhang, Y., et al. 2016, ApJL, 821, L3
Tanaka, K. E. I., Zhang, Y., Hirota, T., et al. 2020, ApJL, 900, L2
Taniguchi, K., Sanhueza, P., Olguin, F. A., et al. 2023, ApJ, 950, 57

Tsuribe, T., & Inutsuka, S.-i. 1999, ApJ, 526, 307
Vaillancourt, J. E. 2006, PASP, 118, 1340
Wang, K., Zhang, Q., Testi, L., et al. 2014, MNRAS, 439, 3275
Wells, M. R. A., Beuther, H., Molinari, S., et al. 2024, A&A, 690, A185
Xu, F.-W., Wang, K., Liu, T., et al. 2023, MNRAS, 520, 3259
Zapata, L. A., Fernández-López, M., Sanhueza, P., et al. 2024, ApJ, 974, 257
Zhang, S., Cyganowski, C. J., Henshaw, J. D., et al. 2024, MNRAS, 533,
    1075
Zhang, Q., Wang, Y., Pillai, T., & Rathborne, J. 2009, ApJ, 696, 268
Zhang, Y., Tan, J. C., Tanaka, K. E. I., et al. 2019, NatAs, 3, 517